

Floating Dropsondes With DGPS Receiver for Real-Time Typhoon Monitoring

Shiung-Chi Tsai and Jean-Fu Kiang

Abstract—Both a geometrical correction and a residual error correction schemes are proposed to improve the positioning accuracy of a three-frequency differential global positioning system (DGPS) on the order of centimeters, using 1 s of received data, and the baseline can be up to 120 km. An ad hoc network of floating dropsondes bearing DGPS receivers is proposed to monitor the progress of a typhoon in real time. An empirical typhoon model is adopted to simulate the deployment of such a network in typhoon Morakot and hurricane Katrina to verify its feasibility.

Index Terms—Global positioning system, hurricanes, remote monitoring, typhoons.

I. INTRODUCTION

TYPHOONS, also called tropical cyclones or hurricanes, routinely wreak havoc and cause serious damages to many areas around the world every year. Proper evacuation procedure can be taken if a strong typhoon is anticipated, which requires more real-time on-site information. Many technologies have been developed to probe such information, for example, Doppler radar [1], synthetic aperture radar [2], special sensor microwave/imager aboard satellites [3]–[8], and so on.

A typhoon absorbs most of its heat energy from warm sea surfaces [9]–[12], and the process is affected by the wind field, humidity, and temperature close to the sea surface, from tens of meters to 1.2 km at altitude [13], [14]. Clouds also have tremendous impacts on typhoon development [15], [16], and dropsondes have been deployed to measure the cloud structures within a typhoon, from hundreds of meters to 10 km at height [17].

Major rainbands of a typhoon usually extend from the eye-wall to about 100 km from the center [18], [19]. Convective cells are accompanied by overturning updrafts and low-level downdrafts up to 10 km above the sea level [20]. Such vertical convective motions within the rainband can be measured with Doppler radars or dropsondes carrying GPS receiver [20]–[23].

The project of dropsonde observations for typhoon surveillance near the Taiwan region has been executed near Taiwan since 2003, after its predecessor [24], in which dropsondes bearing GPS receiver are deployed with planes to monitor the typhoon progress [25]–[28]. In [29], emissivity spectra

are retrieved by applying the FAST emissivity model version 3 to the wind parameters recorded with GPS dropsondes and are compared to the emissivity retrieved from coincident WINDSAT measurements.

In [30], airborne light detection and ranging (LIDAR) technique is used to build digital elevation models, where the GPS positioning of the LIDAR instrument is often the limiting factor, with the typical resolution around 10–30 cm.

A fast-convergent algorithm is required to calculate the coordinates of the floating dropsondes in nearly real time. In [31], 5 min of data at a single frequency is used. With a short baseline of 2 km, the deviation in the height coordinate ranges from 1.6 to 3.3 cm. With a baseline of 102 km, such deviation ranges from 27 to 175 cm. In [32], the deviation of the coordinates is $-20, 30, 4$ cm with a baseline of 1.2 km and the sampling time of 30 s. In [33], the rms deviation is about 10 cm in the North Atlantic and 30 cm in the sea-ice region north of Greenland, with baselines of many hundreds of kilometers.

In [34], a differential global positioning (DGPS) technique is tested on a platform at the speed of 20–100 km/h and with the baseline of 1000 km, and the accuracy of 1–3 m is achieved in real time. In [35], a method is proposed to improve the resolution of a fast carrier-phase ambiguity with baselines up to 200 km. The technique is demonstrated over 1 h of data from four of the five reference stations to obtain precise ionospheric corrections. The residual effects still limit the accuracy to 10 cm after such corrections. In [36], the spatial correlation of both ionospheric and tropospheric propagation delays is used to improve the accuracy to about 2–10 cm, using 30 s of data over baselines of 150–300 km.

In this paper, an effective DGPS algorithm with geometrical correction and residual error correction schemes is proposed to estimate the coordinates of dropsondes using 1 s of data, over baseline up to 120 km. An ad hoc DGPS receiver network is proposed to improve the positioning accuracy of the dropsondes so that the wind field of a typhoon can be measured. Conventional chutes of dropsondes are replaced by weather balloons to extend the operational time of the dropsondes, which have not been used on dropsondes before [37], [38]. Proper radii of balloons are chosen so that the dropsondes can stay at different heights within a typhoon to measure the height profile of different weather parameters. Deployment scheme of dropsondes and airplane route have also been simulated to achieve a more uniform spatial distribution of dropsondes.

This paper is organized as follows. The DGPS algorithm is presented in Section II, an empirical wind-field model of typhoons, and the kinematics of floating dropsondes are analyzed in Sections III and IV, respectively. The simulation results

Manuscript received June 21, 2010; accepted March 31, 2011. Date of publication May 19, 2011; date of current version October 28, 2011. This work was supported by the National Science Council, Taiwan, under Contract NSC 97-2221-E-002-142.

The authors are with the Department of Electrical Engineering and the Graduate Institute of Communication Engineering, National Taiwan University, Taipei 106, Taiwan (e-mail: jfkiang@cc.ee.ntu.edu.tw).

Digital Object Identifier 10.1109/TGRS.2011.2144608

based on the scenarios of typhoon Morakot and Hurricane Katrina are demonstrated in Section V, followed by the conclusion.

II. DGPS ALGORITHM

The ionospheric and tropospheric perturbations to the GPS signals received at two close-by GPS receivers can be compensated to some extent by applying the DGPS technique [39]–[42]. The carrier phase ϕ and the pseudorange ρ between a GPS satellite and a receiver are defined as [39], [40], [43]

$$\phi = r + I_\phi + T_\phi + c(\delta t^s - \delta t_u) - \lambda N_\phi + \varepsilon_\phi$$

$$\rho = r + I_\rho + T_\rho + c(\delta t^s - \delta t_u) + \varepsilon_\rho$$

where λ is the wavelength of the GPS signal, r is the distance between the satellite and the receiver, $I_{\phi,\rho}$ and $T_{\phi,\rho}$ are the delays in the ionosphere and the troposphere, respectively, c is the speed of light in free space, δt^s and δt_u are the clock errors at the satellite and the receiver, respectively, N_ϕ is the integer ambiguity, and $\varepsilon_{\phi,\rho}$ are the noises embedded in the carrier phase and the pseudorange, respectively. Note that $I_\phi = -I_\rho$ and $T_\phi = T_\rho$ [39].

Define the double difference of the carrier phase and the pseudorange at two receivers associated with satellites k and ℓ as

$$\Delta\phi = \phi_{ur}^{(k\ell)} = r_{ur}^{(k\ell)} - I_{ur}^{(k\ell)} + T_{ur}^{(k\ell)} - \lambda N_{ur}^{(k\ell)} + \varepsilon_{\phi,ur}^{(k\ell)}$$

$$\simeq r_{ur}^{(k\ell)} - \lambda N_{ur}^{(k\ell)} + \varepsilon_{\phi,ur}^{(k\ell)}$$

$$\Delta\rho = \rho_{ur}^{(k\ell)} = r_{ur}^{(k\ell)} + I_{ur}^{(k\ell)} + T_{ur}^{(k\ell)} + \varepsilon_{\rho,ur}^{(k\ell)}$$

$$\simeq r_{ur}^{(k\ell)} + \varepsilon_{\rho,ur}^{(k\ell)}$$

where $\zeta_{ur}^{(k\ell)} = \zeta_{ur}^{(k)} - \zeta_{ur}^{(\ell)}$ with $\zeta = \phi, \rho, r, I_\rho, T_\rho, N_\phi, \varepsilon_\rho, \varepsilon_\phi$ and the superscripts $k\ell$ and the subscripts ur are indices to relevant GPS satellites and receivers, respectively. The double differences associated with I_ρ and T_ρ have been neglected under the approximation that $I_{\rho,u} \simeq I_{\rho,r}$ and $T_{\rho,u} \simeq T_{\rho,r}$ when the user and the reference receivers are not too far apart.

A. Determination of Ambiguities at Three Carriers

The double difference of carrier phase and pseudorange measurement vectors at frequency f_α can be decomposed into

$$\begin{aligned} \Delta\bar{\phi}_\alpha &= \Delta\bar{r} + \Delta\bar{T} - \Delta\bar{I}_\alpha - \lambda_\alpha \Delta\bar{N}_\alpha + \Delta\bar{\varepsilon}_\phi \\ \Delta\bar{\rho}_\alpha &= \Delta\bar{r} + \Delta\bar{T} + \Delta\bar{I}_\alpha + \Delta\bar{\varepsilon}_\rho \end{aligned} \quad (1)$$

where

$$\begin{aligned} \Delta\bar{\phi}_\alpha &= [\phi_{ur,\alpha}^{(21)}, \phi_{ur,\alpha}^{(31)}, \dots, \phi_{ur,\alpha}^{(K1)}]^t \\ \Delta\bar{\rho}_\alpha &= [\rho_{ur,\alpha}^{(21)}, \rho_{ur,\alpha}^{(31)}, \dots, \rho_{ur,\alpha}^{(K1)}]^t \end{aligned} \quad (2)$$

are the double-difference carrier phase and pseudorange measurement vectors associated with K satellites at frequency f_α . Three carrier frequencies at $f_1 = 1575.42$ MHz, $f_2 = 1227.6$ MHz, and $f_5 = 1176.45$ MHz are considered, which are indicated by $\alpha = 1, 2,$ and $5,$ respectively. Similarly, define

$$\Delta\bar{\zeta}_\alpha = [\zeta_{ur,\alpha}^{(21)}, \zeta_{ur,\alpha}^{(31)}, \dots, \zeta_{ur,\alpha}^{(K1)}]^t$$

with $\zeta = r, T_\rho, I_\rho, N_\phi, \varepsilon_\phi, \varepsilon_\rho$. The subscript α is removed if the quantity is independent of the frequency. The integer ambiguities $\Delta\bar{N}_\alpha$ in (1) can be estimated using the three-carrier ambiguity resolution [44], [45].

Define the combined double-difference phase and pseudorange measurement vectors as

$$\Delta\bar{\phi}_{(i,j,k)} = \frac{if_1\Delta\bar{\phi}_1 + jf_2\Delta\bar{\phi}_2 + kf_5\Delta\bar{\phi}_5}{if_1 + jf_2 + kf_5}$$

$$\Delta\bar{\rho}_{(i,j,k)} = \frac{if_1\Delta\bar{\rho}_1 + jf_2\Delta\bar{\rho}_2 + kf_5\Delta\bar{\rho}_5}{if_1 + jf_2 + kf_5}$$

where the integers $i, j,$ and k are properly selected [44], [45]. Define the combined integer ambiguity and combined wavelength as

$$\begin{aligned} \Delta\bar{N}_{(i,j,k)} &= i\Delta\bar{N}_1 + j\Delta\bar{N}_2 + k\Delta\bar{N}_5 \\ \lambda_{(i,j,k)} &= \frac{c}{if_1 + jf_2 + kf_5}. \end{aligned} \quad (3)$$

The extrawidelane (EWL) is a geometry-free determination, derived to compute the ambiguity [44], [45]

$$\Delta\bar{N}_{(0,1,-1)} = \text{round} \left\{ \frac{\Delta\bar{\rho}_{(0,1,1)} - \Delta\bar{\phi}_{(0,1,-1)}}{\lambda_{(0,1,-1)}} \right\}.$$

Another EWL is defined as

$$\begin{aligned} \begin{bmatrix} \Delta\bar{\phi}_{(0,1,-1)} + \lambda_{(0,1,-1)}\Delta\bar{N}_{(0,1,-1)} \\ \Delta\bar{\phi}_{(1,-6,5)} \end{bmatrix} &= \begin{bmatrix} \bar{A} & 0 \\ \bar{A} & \lambda_{(1,-6,5)}\bar{I} \end{bmatrix} \\ &\times \begin{bmatrix} \bar{x}_{ur} \\ \Delta\bar{N}_{(1,-6,5)} \end{bmatrix} \end{aligned}$$

from which $\Delta\bar{N}_{(1,-6,5)}$ can be determined using the least squares method, where $\bar{x}_{ur} = \bar{x}_u - \bar{x}_r$ is the relative position vector to be estimated, \bar{I} is an identity matrix

$$\bar{A} = \begin{bmatrix} \hat{s}_r^{(2)} - \hat{s}_r^{(1)} \\ \hat{s}_r^{(3)} - \hat{s}_r^{(1)} \\ \vdots \\ \hat{s}_r^{(K)} - \hat{s}_r^{(1)} \end{bmatrix}$$

is the observational matrix, and $\hat{s}_r^{(k)}$ is the unit vector pointing from the reference receiver to satellite k . Also, a widelane is defined as

$$\begin{aligned} \begin{bmatrix} \Delta\bar{\phi}_{(0,1,-1)} + \lambda_{(0,1,-1)}\Delta\bar{N}_{(0,1,-1)} \\ \Delta\bar{\phi}_{(4,0,-3)} \end{bmatrix} \\ = \begin{bmatrix} \bar{A} & 0 \\ \bar{A} & \lambda_{(4,0,-3)}\bar{I} \end{bmatrix} \begin{bmatrix} \bar{x}_{ur} \\ \Delta\bar{N}_{(4,0,-3)} \end{bmatrix} \end{aligned}$$

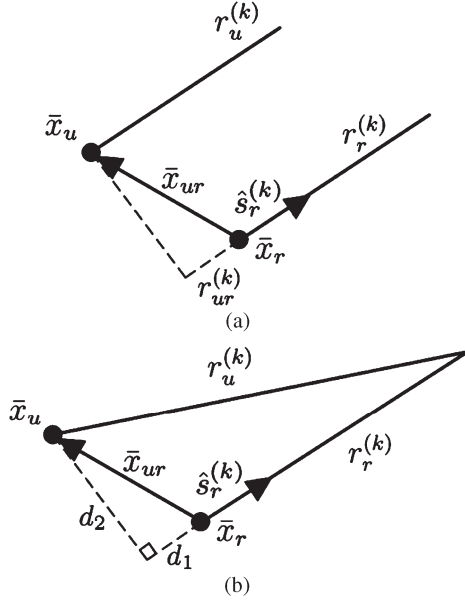


Fig. 1. Geometry for single-difference measurements. (a) With a short baseline. (b) With a long baseline.

from which the ambiguity $\Delta\bar{N}_{(4,0,-3)}$ can be determined using the least squares method.

At last, the ambiguities at f_1 , f_2 , and f_5 can be derived based on (3) as

$$\begin{bmatrix} \Delta\bar{N}_{(1,0,0)} \\ \Delta\bar{N}_{(0,1,0)} \\ \Delta\bar{N}_{(0,0,1)} \end{bmatrix} = \begin{bmatrix} -18 & -3 & 1 \\ -23 & -4 & 1 \\ -24 & -4 & 1 \end{bmatrix} \begin{bmatrix} \Delta\bar{N}_{(0,1,-1)} \\ \Delta\bar{N}_{(1,-6,5)} \\ \Delta\bar{N}_{(4,0,-3)} \end{bmatrix}.$$

B. Geometrical Correction

Fig. 1(a) shows the scheme of single-difference measurement with a short baseline, where the two vectors are almost parallel. However, with a long baseline as shown in Fig. 1(b), the parallel approximation between these two vectors are no longer accurate enough. In such case, $r_u^{(k)}$ can be expressed in terms of $r_r^{(k)}$ as

$$\begin{aligned} r_u^{(k)} &= \left\{ \left[r_r^{(k)} \right]^2 + \bar{x}_{ur} \cdot \bar{x}_{ur} + 2r_r^{(k)} \left[-\bar{x}_{ur} \cdot \hat{s}_r^{(k)} \right] \right\}^{1/2} \\ &\simeq r_r^{(k)} - \bar{x}_{ur} \cdot \hat{s}_r^{(k)} + \frac{\bar{x}_{ur} \cdot \bar{x}_{ur}}{2r_r^{(k)}} - \frac{[\bar{x}_{ur} \cdot \hat{s}_r^{(k)}]^2}{2r_r^{(k)}} \\ &\quad + \frac{[\bar{x}_{ur} \cdot \hat{s}_r^{(k)}] (\bar{x}_{ur} \cdot \bar{x}_{ur})}{2[r_r^{(k)}]^2} - \frac{[\bar{x}_{ur} \cdot \bar{x}_{ur}]^2}{8[r_r^{(k)}]^3} \\ &\quad - \frac{1}{2} \left[\frac{\bar{x}_{ur} \cdot \hat{s}_r^{(k)}}{r_r^{(k)}} \right]^3 + \frac{3}{4} \left[\frac{\bar{x}_{ur} \cdot \hat{s}_r^{(k)}}{r_r^{(k)}} \right]^2 \frac{\bar{x}_{ur} \cdot \bar{x}_{ur}}{[r_r^{(k)}]^2} + \dots \end{aligned}$$

Hence, the double-difference $r_{ur}^{(k\ell)}$ can be expressed as

$$\begin{aligned} r_{ur}^{(k\ell)} &= \left[r_u^{(k)} - r_r^{(k)} \right] - \left[r_u^{(\ell)} - r_r^{(\ell)} \right] \\ &= - \left[\hat{s}_r^{(k)} - \hat{s}_r^{(\ell)} \right] \cdot \bar{x}_{ur} \\ &\quad + \left\{ \frac{\bar{x}_{ur} \cdot \bar{x}_{ur}}{2r_r^{(k)}} - \frac{[\bar{x}_{ur} \cdot \hat{s}_r^{(k)}]^2}{2r_r^{(k)}} \right. \\ &\quad + \frac{[\bar{x}_{ur} \cdot \hat{s}_r^{(k)}] (\bar{x}_{ur} \cdot \bar{x}_{ur})}{2[r_r^{(k)}]^2} - \frac{(\bar{x}_{ur} \cdot \bar{x}_{ur})^2}{8[r_r^{(k)}]^3} \\ &\quad \left. - \frac{1}{2} \left[\frac{\bar{x}_{ur} \cdot \hat{s}_r^{(k)}}{r_r^{(k)}} \right]^3 + \frac{3}{4} \left[\frac{\bar{x}_{ur} \cdot \hat{s}_r^{(k)}}{r_r^{(k)}} \right]^2 \frac{\bar{x}_{ur} \cdot \bar{x}_{ur}}{[r_r^{(k)}]^2} \right\} \\ &\quad - \left\{ \frac{\bar{x}_{ur} \cdot \bar{x}_{ur}}{2r_r^{(\ell)}} - \frac{[\bar{x}_{ur} \cdot \hat{s}_r^{(\ell)}]^2}{2r_r^{(\ell)}} + \frac{[\bar{x}_{ur} \cdot \hat{s}_r^{(\ell)}] (\bar{x}_{ur} \cdot \bar{x}_{ur})}{2[r_r^{(\ell)}]^2} \right. \\ &\quad \left. - \frac{(\bar{x}_{ur} \cdot \bar{x}_{ur})^2}{8[r_r^{(\ell)}]^3} + \frac{1}{2} \left[\frac{\bar{x}_{ur} \cdot \hat{s}_r^{(\ell)}}{r_r^{(\ell)}} \right]^3 \right. \\ &\quad \left. + \frac{3}{4} \left[\frac{\bar{x}_{ur} \cdot \hat{s}_r^{(\ell)}}{r_r^{(\ell)}} \right]^2 \frac{\bar{x}_{ur} \cdot \bar{x}_{ur}}{[r_r^{(\ell)}]^2} \right\} \\ &= - \left[\hat{s}_r^{(k)} - \hat{s}_r^{(\ell)} \right] \cdot \bar{x}_{ur} + \alpha_{ur}^{(k\ell)}. \end{aligned} \quad (4)$$

Take, for example, if the baseline is 100 km, the first two terms in the braces are about 10^{-4} and the third and the fourth terms in the braces are about 10^{-6} and 10^{-8} , respectively.

Since $|\alpha_{ur}^{(k\ell)}| \ll |[\hat{s}_r^{(k)} - \hat{s}_r^{(\ell)}] \cdot \bar{x}_{ur}|$, (4) can be reduced to

$$r_{ur}^{(k\ell)} = - \left[\hat{s}_r^{(k)} - \hat{s}_r^{(\ell)} \right] \cdot \bar{x}_{ur,0}$$

upon which the least squares method can be applied to get the initial guess $\bar{x}_{ur,0}$.

Next, calculate $\alpha_{ur,1}^{(k\ell)}$ based on the initial guess $\bar{x}_{ur,0}$ as

$$\begin{aligned} \alpha_{ur,1}^{(k\ell)} &= \left\{ \frac{\bar{x}_{ur,0} \cdot \bar{x}_{ur,0}}{2r_r^{(k)}} - \frac{[\bar{x}_{ur,0} \cdot \hat{s}_r^{(k)}]^2}{2r_r^{(k)}} \right. \\ &\quad + \frac{[\bar{x}_{ur,0} \cdot \hat{s}_r^{(k)}] (\bar{x}_{ur,0} \cdot \bar{x}_{ur,0})}{2[r_r^{(k)}]^2} - \frac{(\bar{x}_{ur,0} \cdot \bar{x}_{ur,0})^2}{8[r_r^{(k)}]^3} \left. \right\} \\ &\quad - \left\{ \frac{\bar{x}_{ur,0} \cdot \bar{x}_{ur,0}}{2r_r^{(\ell)}} - \frac{[\bar{x}_{ur,0} \cdot \hat{s}_r^{(\ell)}]^2}{2r_r^{(\ell)}} \right. \\ &\quad \left. + \frac{[\bar{x}_{ur,0} \cdot \hat{s}_r^{(\ell)}] (\bar{x}_{ur,0} \cdot \bar{x}_{ur,0})}{2[r_r^{(\ell)}]^2} - \frac{(\bar{x}_{ur,0} \cdot \bar{x}_{ur,0})^2}{8[r_r^{(\ell)}]^3} \right\}. \end{aligned} \quad (5)$$

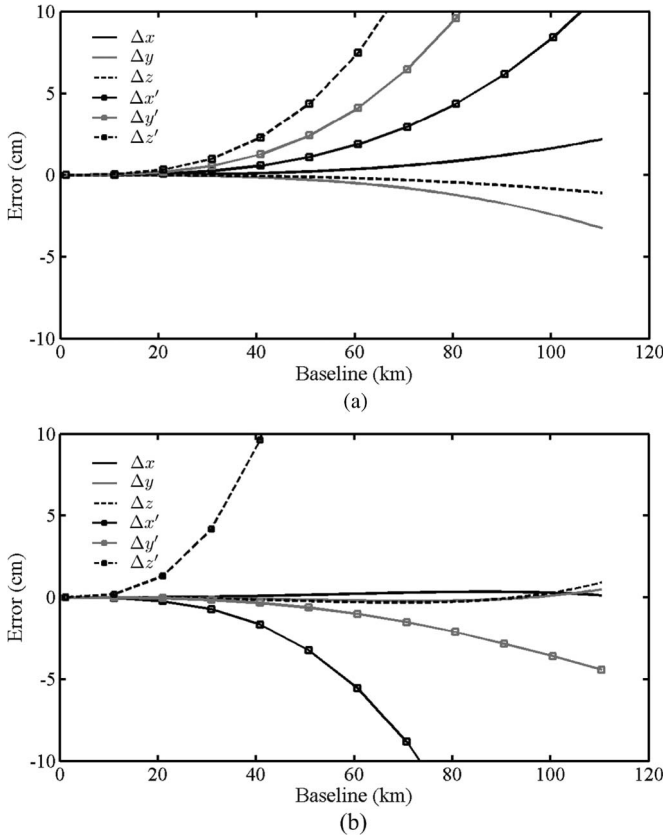


Fig. 2. Position errors without tropospheric error, ionospheric error, or noise. (a) $\theta = 45^\circ$. (b) $\theta = 162^\circ$. Marks indicate the results without residual error correction.

Substitute (5) into (4) to derive

$$r_{ur}^{(k\ell)} - \alpha_{ur,1}^{(k\ell)} = - \left[\hat{s}_r^{(k)} - \hat{s}_r^{(\ell)} \right] \cdot \bar{x}_{ur,1}$$

The least squares method is applied again to get $\bar{x}_{ur,1}$, which is then used to calculate the residual term $\alpha_{ur,2}^{(k\ell)}$. The process is repeated until \bar{x}_{ur} converges.

C. Residual Error Correction

The positions of the dropsondes and the satellites are known in the simulation, and the residual errors after geometrical correction are observed to roughly follow a cubic function of the baseline length $R = |\bar{x}_{ur}|$ as

$$\varepsilon_\alpha(\theta) = a_\alpha(\theta)R^3 \tag{6}$$

where $\alpha = x, y, z$. Fig. 2 shows the position errors based on 1 s of received data, in the absence of tropospheric error, ionospheric error, or noise. The position errors with residual error correction are obviously smaller than those without it.

The coefficients a_α 's are functions of the azimuth angle θ , which is the angle of \bar{x}_{ur} measured from the north. Fig. 3 shows the coefficients based on the constellation status at UTC + 8 = 23 : 30 on August 6, 2009, which remain almost constant over 300 s. These coefficients are associated with a specific constellation status over a specific period of time, and they can be determined *a priori*. In the visionary field trials, the

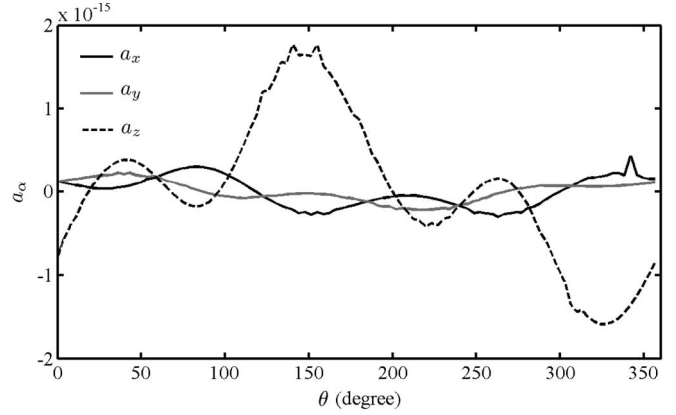


Fig. 3. Coefficients a_α 's as functions of θ , based on the constellation status at UTC + 8 = 23 : 30 on August 6, 2009.

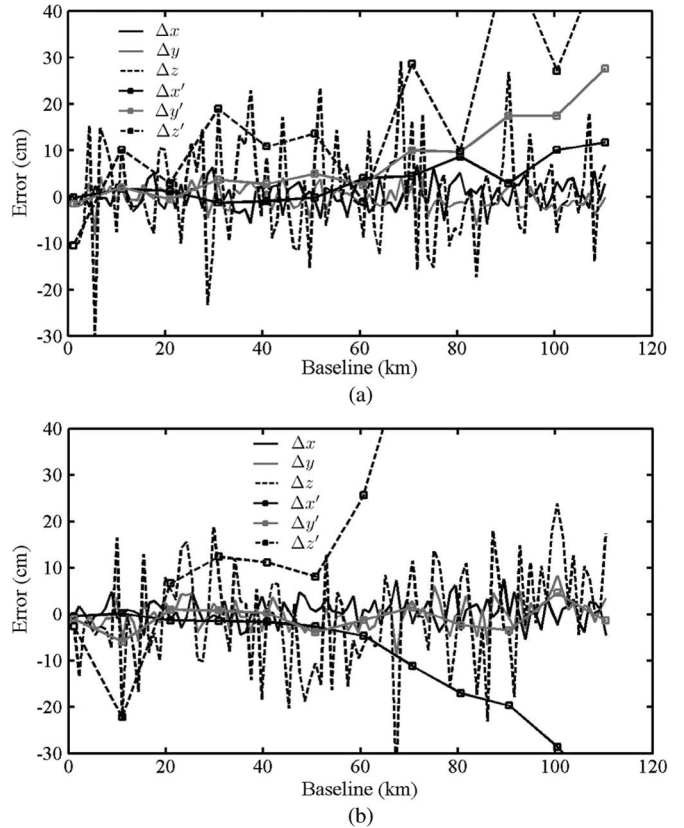


Fig. 4. Position errors without tropospheric or ionospheric error but with noise. (a) $\theta = 45^\circ$. (b) $\theta = 162^\circ$. Marks indicate the results without residual error correction.

baseline length R based on conventional GPS data is sufficient to retrieve the residual errors.

Fig. 4 shows the position errors without tropospheric or ionospheric errors but with the noise, and the receiver position is estimated using 1 s of received data too. Fig. 5 shows the position errors in the presence of tropospheric error, ionospheric error, and noise. It is observed that the troposphere induces more error than the ionosphere does, and the tropospheric error is not completely compensated when the baseline is long. The tropospheric and ionospheric errors can be reduced using

wind speed is approximated as a linear function of the radius ρ , increasing from about 13.87 m/s at the outer rim $R = 250$ km to 32.6 m/s at the inner perimeter of the eyewall $\rho_e = 25$ km. The upward wind speed v_z is about one-thousandth of the azimuthal speed [48].

In region C, the radial and the vertical wind speeds are approximated as $v_{\rho,C}^{(w)} = -10$ and 0 m/s, respectively.

In region D, the radial wind speed $v_{\rho,D}^{(w)}$ increases linearly from $v_{\rho,C}^{(w)}$ m/s at $\rho = \rho_e + a_1$ to zero at $\rho = \rho_e$. The vertical wind speed $v_{z,D}^{(w)}$ ($z = a_3$) is derived under the conservation of mass, where the air density within the typhoon is approximated as a constant. We also make an approximation that the vertical wind speeds in regions D and E are the same as $v_{z,D}^{(w)}$ ($z = a_3$).

Similarly, the radial wind speed in region A, $v_{\rho,A}^{(w)}$ (ρ), is derived by assuming that the mass entering region B is the same as that flowing into region A.

In region B, the vertical wind speed $v_{z,B}^{(w)}$ decreases linearly from $v_{z,E}^{(w)}$ (ρ) at $z = h_1 + a_2$ to zero at $z = h_2$. The radial wind speed decreases linearly from $v_{\rho,A}^{(w)}$ ($\rho = \rho_e + a_1$) at $\rho = \rho_e + a_1$ to zero at $\rho = \rho_e$.

In region F, the vertical wind speed $v_{z,F}^{(w)}$ at $\rho_{m,F} = (R + \rho_2)/2$ is estimated as

$$v_{m,F} = v_{z,F}^{(w)}(\rho_{m,F}) = 0.001v_{\phi}^{(w)}(\rho_{m,F}).$$

The vertical wind speed decreases to zero at $\rho = R$ and $\rho = \rho_2$.

In region G, the radial wind speed $v_{\rho,G}^{(w)}$ at $\rho = \rho_2$ is derived under the conservation of mass. The radial wind speed decreases linearly from $v_{\rho_2,G}^{(w)}$ at $\rho = \rho_2$ to zero at $\rho = R$. The vertical wind speed $v_{z,G}^{(w)}$ decreases linearly from $v_{z,F}^{(w)}$ at $z = h_1$ to zero at $z = h_1 + a_2$.

In region H, the vertical wind speed is approximated as

$$v_{z,H}^{(w)}(\rho) = \begin{cases} v_{m,H} \left(\frac{\rho_2 - \rho}{\rho_2 - \rho_{m,H}} \right), & \rho_{m,H} \leq \rho \leq \rho_2 \\ v_{m,H} \left(\frac{\rho_2 - 2\rho_{m,H} + \rho}{\rho_2 - \rho_{m,H}} \right), & \rho_1 \leq \rho \leq \rho_{m,H} \end{cases}$$

where $\rho_{m,H} = (\rho_1 + \rho_2)/2$ and $v_{m,H}$ are derived under the conservation of mass.

In region I, the radial wind speed decreases linearly from $v_{\rho_2,I}^{(w)}$ at $\rho = \rho_2$ to zero at $\rho = \rho_1$. The vertical wind speed $v_{z,I}^{(w)}$ is assumed to decrease linearly from $v_{z,H}^{(w)}$ at $z = h_1$ to zero at $z = h_1 + a_2$.

The wind-speed distributions in regions J, K, L, and M are derived in a similar manner to those in regions F, G, H, and I.

IV. KINEMATICS OF DROPSONDES

The motion of a balloon is determined by the gravity, buoyancy, and air resistance. The air resistance of a chute or a balloon under low speed of wind is [49]–[51]

$$\bar{F}_{d,l} = -\hat{u}_{dw} k v_{dw}$$

where v_{dw} and \hat{u}_{dw} are the magnitude and direction, respectively, of the dropsonde velocity with respect to the wind and

$$k = \frac{1}{2} C_d \rho_{\text{air}} A$$

with C_d being the drag coefficient, ρ_{air} being the air density, and A being the equivalent area of the chute or balloon.

Under high speed of wind, the air resistance becomes

$$\bar{F}_{d,h} = -\hat{u}_{dw} k v_{dw}^2.$$

For a typical dropsonde equipped with a circle chute, weighing less than 400 g, the drag coefficient is about 0.47 [52], and the equivalent area is about 706.8 cm² [53].

A weather balloon is expected to have a longer gliding time than a chute. The buoyancy of a balloon is

$$\bar{F}_b = -(\rho_{\text{air}} - \rho_{\text{in}}) V \bar{g}$$

where ρ_{in} is the density of air inside the balloon with volume V and \bar{g} is the gravity.

The acceleration of a balloon with mass m is determined by all the exerted forces as

$$\bar{a}(t) = \frac{\bar{F}_d + \bar{F}_b}{m} - \hat{z}g$$

and its velocity and displacement vectors at time instant t can be derived as

$$\begin{aligned} \bar{v}^{(d)}(t) &= \bar{v}^{(d)}(t_0) + \int_{t_0}^t \bar{a}(t') dt' \\ \bar{r}^{(d)}(t) &= \bar{r}^{(d)}(t_0) + \int_{t_0}^t \bar{v}^{(d)}(t') dt' \end{aligned}$$

The dropsonde reaches a terminal velocity when $\bar{a}(t) = 0$.

The density of air can be expressed as [54]

$$\rho_{\text{air}} = \frac{pM}{RT}$$

where p (in pascals) is the pressure at altitude h (in meters), $M = 28.9644$ g/mol is the molecular weight of air, $R = 8.31432$ J/mol/K is the gas constant, and $T = T_0 - Lh$ (K) is the temperature, with the standard temperature at the sea level $T_0 = 288.15$ K and the temperature lapse rate $L = 0.0065$ K/m. The pressure is also a function of h as

$$p = p_0 \left(1 - \frac{Lh}{T_0} \right)^{gM/(RL)}$$

where $p_0 = 101325$ (Pa) is the standard atmospheric pressure at the sea level.

By applying all these kinematic equations, the steady height of a balloon with specific radius can be determined, as shown in Fig. 10.

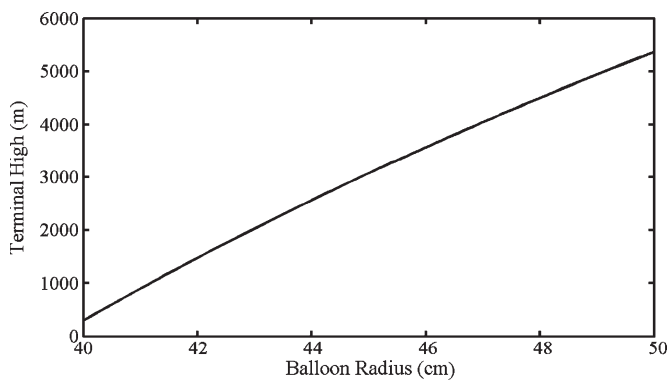


Fig. 10. Steady height of a balloon versus its radius, assuming that the payload weighs 400 g.

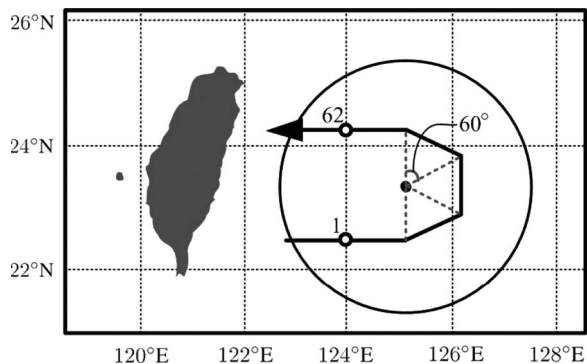


Fig. 11. Simulated flight path over typhoon Morakot. The gray dashed line is 150 km long.

V. RESULTS AND DISCUSSIONS

In this section, simulation results are presented to demonstrate the feasibility of deploying floating dropsondes with DGPS receivers in the scenarios of typhoon Morakot around Taiwan in early August 2009 [55] and hurricane Katrina around Louisiana in late August 2005 [56].

A. Typhoon Morakot

Fig. 11 shows the simulated flight path over typhoon Morakot. The airplane flies at 720 km/h, 12 km above the mean sea level, and the total flight time is about 1 h. A total of 62 dropsondes are deployed along the flight path, with one dropsonde every minute. The radii of balloons are chosen to make them stay from slightly above the sea level to the height of 6 km. The first dropsonde is dropped at 20:30 local time (UTC + 8) on August 6, 2009 when the typhoon center is at 23.5° N, 125.1° E, with a radius of about 250 km.

Figs. 12 and 13 show the distributions of dropsondes in the horizontal and the vertical planes, respectively, at 23:30 local time. Each dropsonde is labeled by an integer to indicate its order of dropping. These dropsondes are drifted into nine clusters, and the one near the center of each cluster is chosen as the reference station in that cluster.

The positioning accuracy is better when the dropsondes are closer to one another, as in cluster one, than when the dropsondes spread farther apart, as in cluster nine. Figs. 14 and 15 show the position errors of dropsonde 43 in cluster one

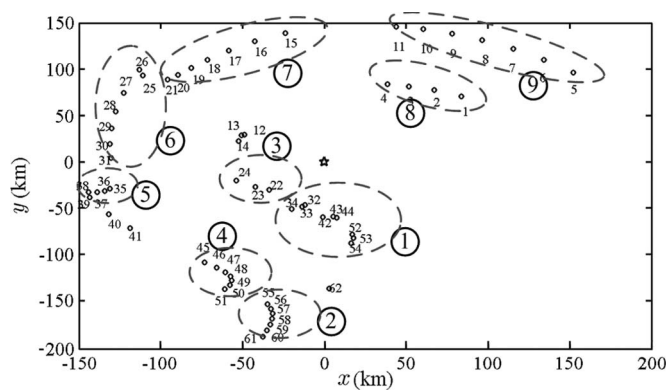


Fig. 12. Horizontal distribution of dropsondes at UTC + 8 = 23 : 30 on August 6, 2009. The star marks the eye of typhoon Morakot.

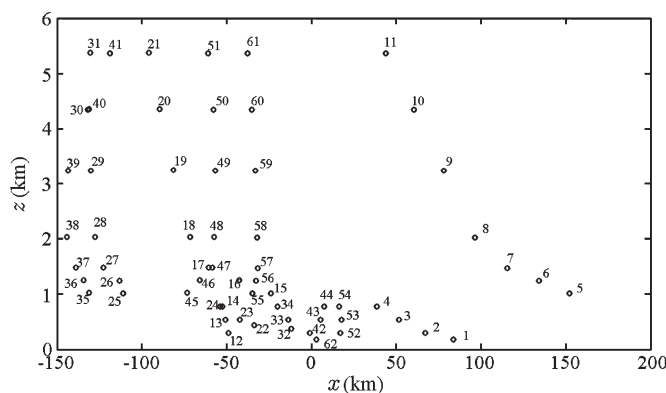


Fig. 13. Vertical distribution of dropsondes at UTC + 8 = 23 : 30 on August 6, 2009.

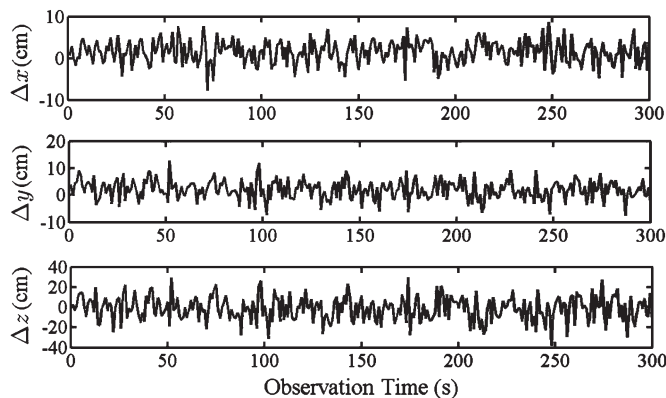


Fig. 14. Position errors of dropsonde 43. Its baseline ranges from 2.43 to 2.73 km, starting at UTC + 8 = 23 : 30 on August 6, 2009. The standard deviations over 300 s are $\sigma_x = 2.78$ cm, $\sigma_y = 3.56$ cm, and $\sigma_z = 12.25$ cm.

and dropsonde 5 in cluster nine, respectively. The ionospheric and tropospheric errors are not completely compensated due to the long baseline [35], [36].

Due to the random nature of wind blow, the receiver antenna may swing and rotate about the center of mass of the whole dropsonde module, which induces a phase variation in the received signal. If a directional antenna like a horn is used, the phase and even the amplitude of the received signal will change when the antenna is rotated by the wind. If an omnidirectional antenna is used, the amplitude of the received signal

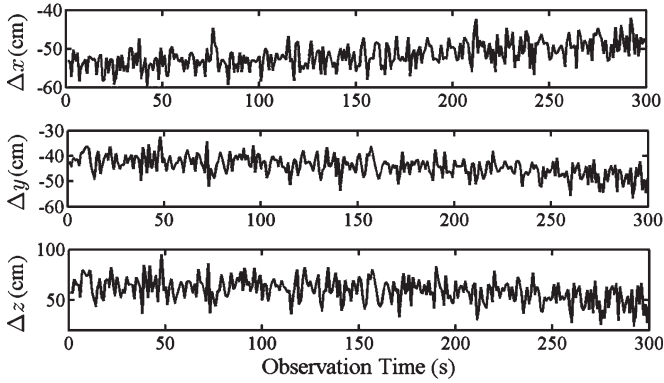


Fig. 15. Position errors of dropsonde 5. Its baseline ranges from 65.99 to 109.05 km, starting at UTC + 8 = 23 : 30 on August 6, 2009. The standard deviations over 300 s are $\sigma_x = 3.32$ cm, $\sigma_y = 4.11$ cm, and $\sigma_z = 12.30$ cm.

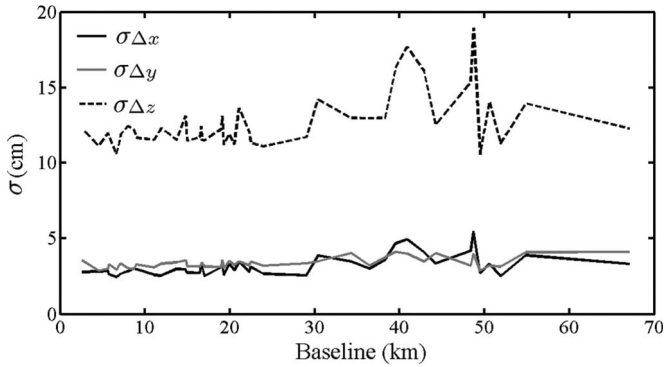


Fig. 16. Standard deviation of position error of all 62 dropsondes at different baselines.

will become independent of the incident direction. If such an omnidirectional antenna is properly designed, including the polarization effect, so that its phase center is close to its physical center, the antenna rotation about its physical center will cause only insignificant phase variation. In the simulation, such phase variation can be incorporated into the phase error term.

We may also contemplate a situation that the antenna rotates about an axis passing through the center of mass of the whole dropsonde module, then the position estimated with the algorithm will be that of the antenna. If the antenna is placed close to or, better off, at the center of mass, the estimated position will be that of the center of mass of the dropsonde module. There must be many practical aspects of implementation not covered in this paper, which may trigger the interest of scientists and engineers studying in this field.

Figs. 16 and 17 show the standard deviations and the averages of the position errors of all these 62 dropsondes. The presented data for each dropsonde are derived from 300 position errors, with one error evaluation per second. The standard deviations in the vertical direction are usually larger than those in the horizontal ones. The average position error increases with the baseline, mainly due to the incomplete compensation of ionospheric and tropospheric errors over a long baseline, even under the double-difference scheme.

Although the position errors become large over a long baseline, the displacement of a dropsonde between two time

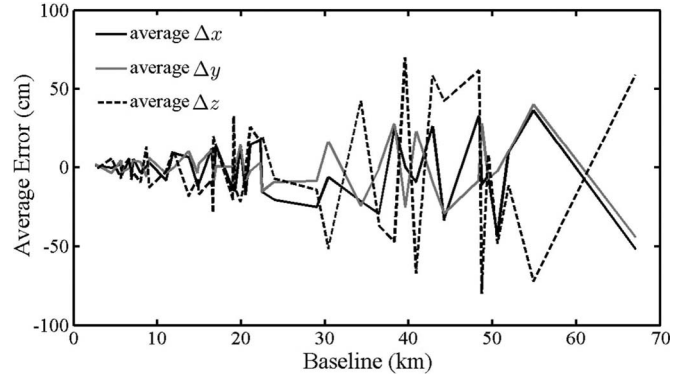


Fig. 17. Average of position error of all 62 dropsondes at different baselines.

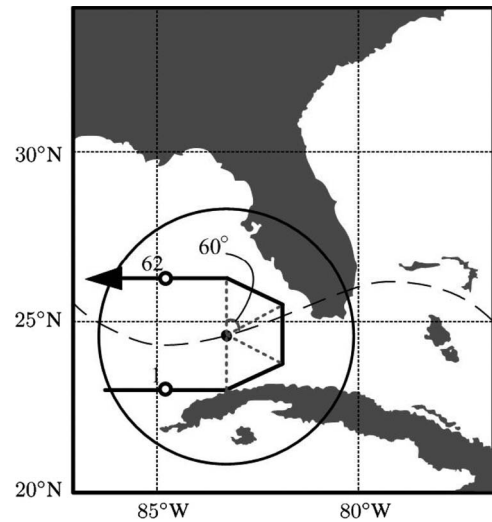


Fig. 18. Simulated flight path over hurricane Katrina. The gray dashed line is 150 km long.

instants, which measures 1 s, can still be estimated accurately enough because the position errors are almost cancelled when taking the difference of the estimated positions at these two instants.

The positions of the reference stations can be estimated using conventional GPS technique or using the DGPS technique by referring to another known reference station.

B. Hurricane Katrina

Fig. 18 shows the simulated flight path over hurricane Katrina. The airplane flies at the speed of 720 km/h, 12 km above the mean sea level, and the total flight time is about 1 h. A total of 62 dropsondes are deployed along the flight path, with one dropsonde every minute. The first dropsonde leaves the cargo bay at 15:00 UTC on August 27, 2005 when the typhoon center is at 24.5° N, 85° W, with the radius of about 380 km. Figs. 19 and 20 show the distributions of dropsondes in the horizontal and the vertical planes, respectively, at 18:00 UTC on August 27, 2005.

These dropsondes are drifted into nine clusters, among which cluster five has better positioning accuracy while cluster nine has worse positioning accuracy. Figs. 21 and 22 show the

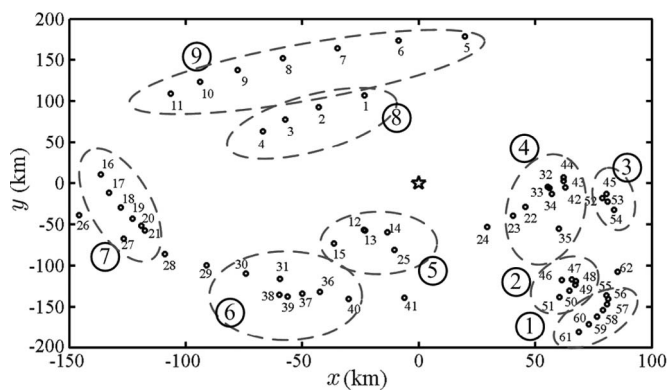


Fig. 19. Horizontal distribution of dropsondes at 18:00 UTC on August 27, 2005. The star marks the eye of hurricane Katrina.

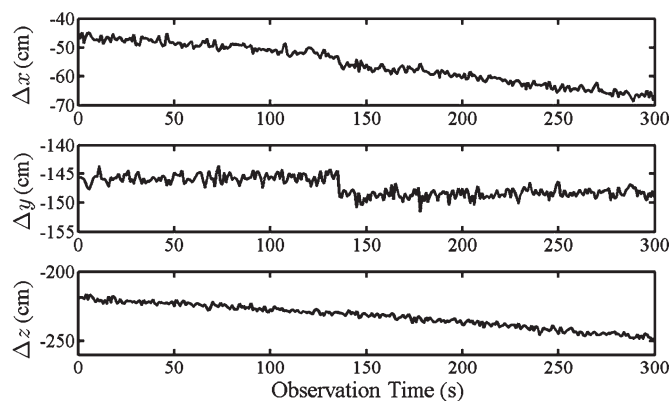


Fig. 22. Position errors of dropsonde 5. Its baseline ranges from 82.57 to 84.11 km, starting at 18:00 UTC on August 27, 2005. The standard deviations over 300 s are $\sigma_x = 6.69$ cm, $\sigma_y = 1.61$ cm, and $\sigma_z = 8.48$ cm.

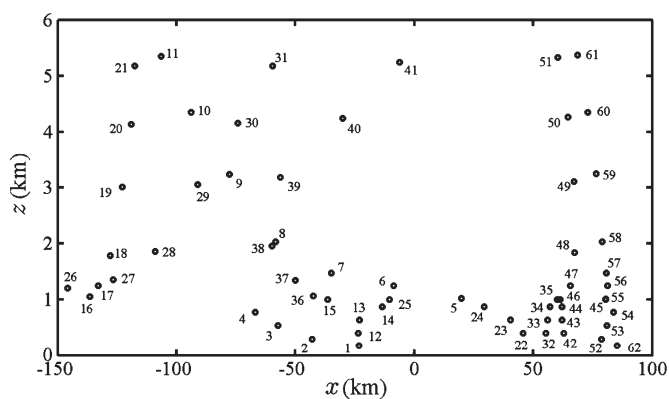


Fig. 20. Vertical distribution of dropsondes at 18:00 UTC on August 27, 2005.

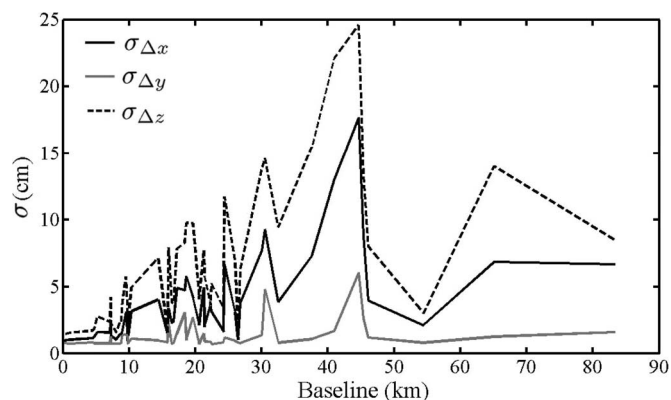


Fig. 23. Standard deviations of position error of all 62 dropsondes.

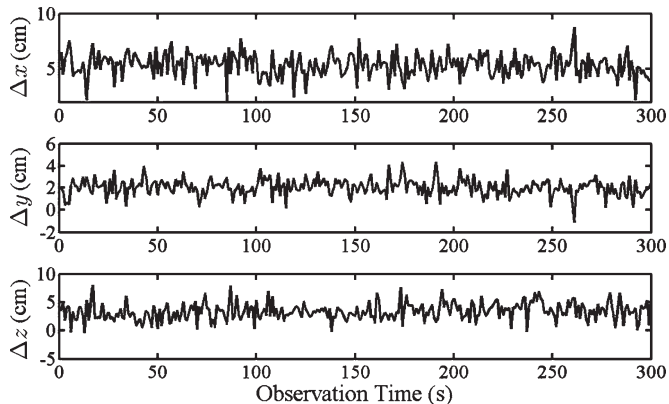


Fig. 21. Position errors of dropsonde 12. Its baseline ranges from 0.99 to 1.16 km, starting at 18:00 UTC on August 27, 2005. The standard deviations over 300 s are $\sigma_x = 1.05$ cm, $\sigma_y = 0.76$ cm, and $\sigma_z = 1.56$ cm.

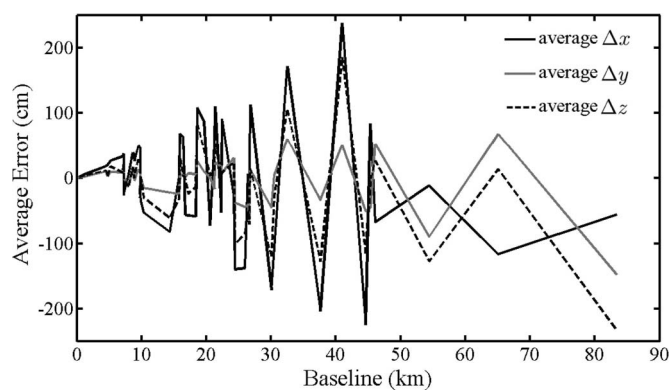


Fig. 24. The averages of position error of all 62 dropsondes.

position errors of dropsonde 12 in cluster five and dropsonde 5 in cluster nine, respectively. Figs. 23 and 24 show the standard deviations and the averages of position errors of all these 62 dropsondes over the observation time of 300 s. It is observed that the average of position errors increases with the baseline.

Although the position errors may reach 1–2 m, the displacement of the dropsonde between two subsequent instants can still be estimated accurately because the position errors are almost cancelled when subtracting the estimated position vectors at these two instants. As for measuring the other weather param-

eters in the hurricane, this level of positioning accuracy is fair enough.

The positioning accuracy in this demonstration is worse than that in typhoon Morakot. Fig. 25 shows the positions of the on-sight GPS satellites at 18:00 UTC on August 27, 2005. The origin indicates the hurricane center, and the difference of elevation angle between two adjacent circles is 15°. It appears that most of the satellites were close to the horizon, which also implies that the ionospheric and tropospheric errors among signals from different satellites are more difficult to cancel.

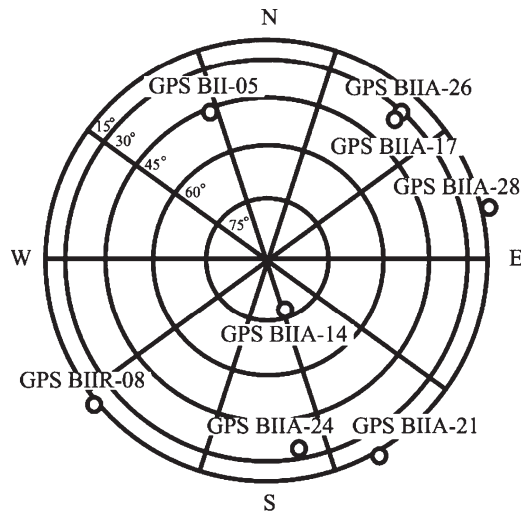


Fig. 25. Positions of GPS satellites at 18:00 UTC on August 27, 2005.

VI. CONCLUSION

A DGPS technique with geometrical and residual error corrections has been proposed, which can achieve the positioning accuracy in centimeters using 1 s of received data, and the baseline can be up to 120 km. An ad hoc network of floating dropsondes has been proposed to monitor typhoon progress in real time, in which the chutes are replaced by weather balloons of designate sizes to extend the observation time of dropsondes at different heights. Plausible application of such a network has been demonstrated under the scenarios of typhoon Morakot and hurricane Katrina. Positioning errors of the dropsondes are analyzed to assess the feasibility of measuring the real-time wind-field distribution of typhoons with this network.

REFERENCES

- [1] D. E. Fernandez, E. M. Kerr, A. Castells, J. R. Carswell, S. J. Frasier, P. S. Chang, P. G. Black, and F. D. Marks, "IWRAP: The imaging wind and rain airborne profiler for remote sensing of the ocean and the atmospheric boundary layer within tropical cyclones," *IEEE Trans. Geosci. Remote Sens.*, vol. 43, no. 8, pp. 1775–1787, Aug. 2005.
- [2] A. Reppucci, S. Lehner, J. S. Stellenfleth, and S. Brusch, "Tropical cyclone intensity estimated from wide-swath SAR images," *IEEE Trans. Geosci. Remote Sens.*, vol. 48, no. 1, pp. 1639–1649, Apr. 2010.
- [3] G. W. Felde and M. Glass, "SSM/I brightness temperatures analysis of tropical cyclones," in *Proc. Conf. Hurricanes Tropical Meteor.*, 1991, pp. 400–404.
- [4] M. A. Goodberlet, C. T. Swift, and J. C. Wilkerson, "Remote sensing of ocean surface winds with the Special Sensor Microwave/Imager," *J. Geophys. Res.*, vol. 94, no. C10, pp. 14 547–14 555, 1989.
- [5] M. A. Goodberlet and C. T. Swift, "Ocean surface wind speed measurements of special sensor microwave/imager (SSM/I)," *IEEE Trans. Geosci. Remote Sens.*, vol. 28, no. 5, pp. 823–828, Sep. 1990.
- [6] J. L. Pierce and G. A. Poe, "SSM/I instrument evaluation," *IEEE Trans. Geosci. Remote Sens.*, vol. 28, no. 5, pp. 781–790, Sep. 1990.
- [7] J. D. Hawkins, F. J. Turk, T. F. Lee, and K. Richardson, "Observations of tropical cyclones with the SSMIS," *IEEE Trans. Geosci. Remote Sens.*, vol. 46, no. 4, pp. 901–912, Apr. 2008.
- [8] S.-A. Boukabara, F. Weng, and Q. Liu, "Passive microwave remote sensing of extreme weather events using NOAA-18 AMSUA and MHS," *IEEE Trans. Geosci. Remote Sens.*, vol. 45, no. 7, pp. 2228–2246, Jul. 2007.
- [9] K. A. Emanuel, "An air–sea interaction theory for tropical cyclones, Part I: Steady-state maintenance," *J. Atmos. Sci.*, vol. 43, no. 6, pp. 585–605, 1986.
- [10] K. A. Emanuel, "Thermodynamic control of hurricane intensity," *Nature*, vol. 401, pp. 665–669, Oct. 1999.
- [11] D. K. Miller and K. B. Katsaros, "Satellite-derived surface latent heat fluxes in a rapidly intensifying marine cyclone," *Monthly Weather Rev.*, vol. 120, no. 7, pp. 1093–1107, Jul. 1992.
- [12] S. Crewell, E. Ruprecht, and C. Simmer, "Latent heat flux over the North Atlantic ocean—A case study," *J. Appl. Meteor.*, vol. 30, no. 12, pp. 1627–1635, Dec. 1991.
- [13] M. S. Moss, "Low-level turbulence structure in vicinity of hurricane," *Monthly Weather Rev.*, vol. 106, no. 6, pp. 841–849, Jun. 1978.
- [14] M. S. Moss and F. J. Merceret, "A note on several low layer features in hurricane Eloise (1975)," *Monthly Weather Rev.*, vol. 104, no. 7, pp. 967–971, 1976.
- [15] R. C. Gentry, "Aircraft, spacecraft, satellite and radar observations of hurricane Gladys (1968)," *J. Appl. Meteor.*, vol. 9, no. 6, pp. 837–850, 1970.
- [16] R. G. Fovell and K. L. Corbosiero, "Cloud microphysics impact on hurricane track as revealed in idealized experiments," *J. Appl. Meteor.*, vol. 66, no. 6, pp. 1764–1778, Jun. 2009.
- [17] Z. Z. Luo, G. L. Stephens, K. A. Emanuel, D. G. Vane, N. D. Tourville, and J. M. Haynes, "On the use of cloudsat and MODIS data for estimating hurricane intensity," *IEEE Geosci. Remote Sens. Lett.*, vol. 5, no. 1, pp. 13–16, Jan. 2008.
- [18] G. M. Barnes and E. J. Zipser, "Mesoscale and convective structure of a hurricane rainband," *J. Atmos. Sci.*, vol. 40, no. 9, pp. 2125–2137, Sep. 1983.
- [19] F. D. Marke, "Evaluation of the structure of precipitation in hurricane Allen (1980)," *Monthly Weather Rev.*, vol. 113, pp. 909–930, 1985.
- [20] D. A. Hince and R. A. Houze, Jr., "Kinematic structure of convective-scale elements in the rainbands of Hurricanes Katrina and Rita (2005)," *J. Geophys. Res.*, vol. 113, p. D15 108, Aug. 2008, DOI:10.1029/2007JD009429.
- [21] S. L. Durden, "Airborne polarimetric radar measurements of rainfall profiles," *IEEE Trans. Geosci. Remote Sens.*, vol. 41, no. 9, pp. 2125–2127, Sep. 2003.
- [22] P. H. Hildebrand, W.-C. Lee, A. Walther, C. Frush, M. Randall, E. Loew, R. Neitzel, R. Parsons, J. Testud, F. Baudin, and A. LeCornec, "The ELDORA/ASTRAIA airborne Doppler weather radar: High resolution observations from TOGA COARE," *Bull. Amer. Meteorol. Soc.*, vol. 77, no. 2, pp. 213–232, Feb. 1996.
- [23] A. C. Didlake, Jr. and R. A. Houze, Jr., "Convective-scale downdrafts in the principal rainband of Hurricane Katrina (2005)," *Monthly Weather Rev.*, vol. 137, no. 10, pp. 3269–3293, Oct. 2009.
- [24] R. W. Burpee, J. L. Franklin, S. J. Lord, R. E. Tuleya, and S. D. Aberson, "The impact of Omega dropwindsondes on operational hurricane track forecast models," *Bull. Amer. Meteor. Soc.*, vol. 77, pp. 925–933, Mar. 1996.
- [25] [Online]. Available: <http://typhoon.as.ntu.edu.tw/DOTSTAR/tw/>
- [26] C. C. Wu, P. H. Lin, T. C. Yeh, and S. D. Aberson, "Dropsonde observations for typhoon surveillance near the Taiwan region: An overview," *Bull. Amer. Meteor. Soc.*, vol. 86, pp. 787–790, Jun. 2005.
- [27] T. F. Hock and J. L. Franklin, "The NCAR GPS dropwindsonde," *Bull. Amer. Meteor. Soc.*, vol. 80, no. 3, pp. 407–420, Mar. 1999.
- [28] S. D. Aberson and J. L. Franklin, "Impact on hurricane track and intensity forecasts of GPS dropwindsonde observations from the first-season flights of the NOAA Gulfstream-IV jet aircraft," *Bull. Amer. Meteor. Soc.*, vol. 80, no. 3, pp. 421–427, Mar. 1999.
- [29] S.-A. Boukabara and F. Weng, "Microwave emissivity over ocean in all-weather conditions: Validation using WINDSAT and airborne GPS dropsondes," *IEEE Trans. Geosci. Remote Sens.*, vol. 46, no. 2, pp. 376–384, Feb. 2008.
- [30] M. A. King, "The GPS contribution to the error budget of surface elevations derived from airborne LIDAR," *IEEE Trans. Geosci. Remote Sens.*, vol. 47, no. 3, pp. 874–883, Mar. 2009.
- [31] D. B. M. Alves and J. F. G. Monico, "Modifying the stochastic model to mitigate GPS systematic errors in relative positioning," *Dynamic Planet*, vol. 130, pp. 166–171, 2007.
- [32] O. Jikun and Z. J. Wang, "An improved regularization method to resolve integer ambiguity in rapid positioning using single frequency GPS receivers," *Chin. Sci. Bull.*, vol. 49, no. 2, pp. 196–200, Jan. 2004.
- [33] X. H. Zhang and R. Forsberg, "Assessment of long-range kinematic GPS positioning errors by comparison with airborne laser altimetry and satellite altimetry," *J. Geod.*, vol. 81, no. 3, pp. 201–211, Mar. 2007.
- [34] G. Lachapell, W. Falkenberg, and M. Casey, "Use of phase data for accurate differential GPS kinematic positioning," *J. Geod.*, vol. 61, pp. 367–377, 1987.
- [35] D. Odijk, H. van der Marel, and I. S. Song, "Precise GPS positioning by applying ionospheric corrections from an active control network," *GPS Solutions*, vol. 3, pp. 49–57, 2000.

[36] T. Schuler, "Impact of systematic errors on precise long baseline kinematic GPS positioning," *GPS Solutions*, vol. 10, no. 2, pp. 108–125, May 2006.

[37] [Online]. Available: <http://sites.wff.nasa.gov/code820/>

[38] [Online]. Available: <http://www.ua.nws.noaa.gov/photo.htm>

[39] P. Misra and P. Enge, *Global Positioning System: Signal, Measurements, and Performance*. Lincoln, MA: Ganga-Jamuna Press, 2006.

[40] J. B.-Y. Tsui, *Fundamentals of Global Positioning System Receivers*. Hoboken, NJ: Wiley, 2005.

[41] G. J. Morgan-Owen and G. T. Johnston, "Differential GPS positioning," *IEE Electron. Commun. Eng. J.*, vol. 7, no. 1, pp. 11–21, Feb. 1995.

[42] G. Chen, "GPS kinematic positioning for the airborne laser altimetry at Long Valley, California," M.S. thesis, Dept. Earth, Atmos., Planet. Sci., MIT, Cambridge, MA, 1999.

[43] S. Gilbert and K. Borre, *Linear Algebra, Geodesy, and GPS*. Wellesley, MA: Wellesley-Cambridge Press, 1997.

[44] B. Li, Y. M. Feng, and Y. Z. Shen, "Three carrier ambiguity resolution: Distance-independent performance demonstrated using semi-generated triple frequency GPS signals," *GPS Solutions*, vol. 14, no. 2, pp. 177–184, Mar. 2010.

[45] Y. M. Feng, "GNSS three carrier ambiguity resolution using ionosphere-reduced virtual signals," *J. Geod.*, vol. 82, no. 12, pp. 847–862, Dec. 2008.

[46] K. Emanuel, *Divine Wind: The History and Science of Hurricanes*. New York: Oxford Univ. Press, 2005.

[47] K. A. Emanuel, "An air-sea interaction theory for tropical cyclones Part I: Steady-state maintenance," *J. Atmos. Sci.*, vol. 43, pp. 585–605, 1986.

[48] J. R. Holton, *An Introduction to Dynamic Meteorology*. New York: Elsevier Academic Press, 2004.

[49] A. P. French, *Newtonian Mechanics*, 1st ed. New York: Norton, 1970.

[50] R. A. Serway and J. W. Jewett, *Physics for Scientists and Engineers.*, 6th ed. Pacific Grove, CA: Brooks/Cole, 2004.

[51] P. Tipler, *Physics for Scientists and Engineers: Mechanics, Oscillations and Waves, Thermodynamics*, 5th ed. San Francisco, CA: Freeman, 2004.

[52] B. W. McCormick, *Aerodynamics, Aeronautics, and Flight Mechanics*. New York: Wiley, 1979.

[53] [Online]. Available: <http://www.eol.ucar.edu/isf/facilities/dropsonde/gpsDropsonde.html>

[54] R. J. List, *Smithsonian Meteorological Tables*. Washington: Smithsonian Inst., 1971.

[55] [Online]. Available: <http://photino.cwb.gov.tw/tyweb/tyfnweb/htm/2009morakot.htm>

[56] [Online]. Available: <http://www.nhc.noaa.gov/archive/2005/KATRINA.shtml>

[57] W. H. Schubert, C. M. Rozoff, J. L. Vigh, B. D. McNoldy, and J. P. Kossin, "On the distribution of subsidence in the hurricane eye," *Quart. J. Roy. Meteorol. Soc.*, vol. 133, pp. 595–605, 2007.



Shiung-Chi Tsai was born in Tainan, Taiwan, on January 18, 1986. He received the B.S. degree in electrical engineering from National Chung Cheng University, Chiayi, Taiwan, in 2008 and the M.S. degree in electrical engineering from the Graduate Institute of Communication Engineering, National Taiwan University, Taipei, Taiwan, in 2010.

He is currently with Quanta, Taipei, Taiwan.



Jean-Fu Kiang was born in Taipei, Taiwan, on February 2, 1957. He received the B.S. and M.S. degrees in electrical engineering from National Taiwan University, Taipei, Taiwan, in 1979 and 1981, respectively, and the Ph.D. degree in electrical engineering from the Massachusetts Institute of Technology, Cambridge, in 1989.

He was with Schlumberger-Doll Research, Ridgefield, CT, in 1985 and 1986; IBM Watson Research Center, Yorktown Heights, NY, from 1989 to 1990; Bellcore, Red Bank, NJ, from 1990 to 1992; Siemens Electromedical Systems, Danvers, MA, from 1992 to 1994; and National Chung-Hsing University, Taichung, Taiwan, from 1994 to 1999. He has been a Professor with the Department of Electrical Engineering and the Graduate Institute of Communication Engineering, National Taiwan University, since 1999. He has been interested in electromagnetic applications and system issues, including wave propagation in the ionosphere and the atmosphere, vehicle and satellite navigation, RF module and transceiver design, antennas, dielectric resonator, and sensor technology.